

All-optical switching of photonic entanglement

Matthew A. Hall, Joseph B. Altepeter, and Prem Kumar

Center for Photonic Communication and Computing, EECS Department
Northwestern University, 2145 Sheridan Road, Evanston, IL 60208-3118

Abstract. Future quantum optical networks will require the ability to route entangled photons at high speeds, with minimal loss and added in-band noise, and—most importantly—without disturbing the photons’ quantum state. Here we present an all-optical switch which fulfills these requirements and characterize its performance at the single photon level. It exhibits a 200-ps switching window, 120:1 contrast, 1.5-dB loss, and induces no measurable degradation in the switched photons’ entangled-state fidelity (< 0.002). As a proof-of-principle demonstration of its capability, we use the switch to demultiplex a single quantum channel from a dual-channel, time-division-multiplexed entangled photon stream. Furthermore, because this type of switch couples the temporal and spatial degrees of freedom, it provides an important new tool with which to encode multiple-qubit quantum states on a single photon.

1. Introduction

Switching technologies enable networked rather than point-to-point communications. Next-generation photonic quantum networks will require switches that operate with low loss, low signal-band noise, and *without* disturbing the transmitted photons' spatial, temporal, or polarization degrees of freedom [1]. Additionally, the switch's operational wavelength must be compatible with a low-loss, non-dispersive transmission medium, such as standard optical fiber's 1.3- μm zero-dispersion band [2, 3]. Unfortunately, no previously demonstrated technology [4]–[19] is capable of *simultaneously* satisfying each of the above requirements: waveguide electro-optic modulators (EOMs) [16] and resonators [14, 17] can operate at very high speeds (10 GHz) but completely destroy any quantum information stored in the polarization degree of freedom; micro-electromechanical switches [6, 18] do not degrade the photon's quantum state, but operate at very low speeds (≤ 250 kHz); polarization-independent EOMs [16] can operate at moderate speeds (~ 100 MHz) but with relatively high loss; and finally, traditional 1550-nm devices based on nonlinear-optical fiber loops [7, 19] generate unacceptably high levels of Raman-induced noise photons (> 1 in-band noise photon per 100-ps switching window [20]).

Although the requirements for ultrafast entangled-photon switching are collectively daunting, they describe a device that is capable of selectively coupling the spatial and temporal degrees of photonic quantum information. In other words, a device that can encode multiple-qubit quantum states onto a single photon, enabling quantum communication protocols that exploit high-dimensional spatio-temporal encodings. In this paper we describe the construction and characterization of an all-optical switch which meets each of the aforementioned requirements. Moreover, this switch design is scalable: by its extension one can create devices that are capable of coupling many temporal qubits and many spatial qubits. As a proof-of-principle demonstration of this capability, we utilize the switch to perform a controlled-bit-flip operation on a two-qubit subspace of a two-photon, five-qubit system, where a temporally encoded qubit is used as the control and a spatially encoded qubit is used as the target. This operation is used to demultiplex a single quantum channel from a dual-channel, time-division-multiplexed entangled photon stream encoded into the larger five-qubit space.

1.1. Comparison with existing switching technologies

The aggregate performance of this switch (in terms of loss, speed, and in-band noise) exceeds that of all available alternatives [4]–[19] by orders of magnitude. Fig. 1 shows the relative performance of our switch compared to each of these alternatives in terms of speed (defined in dB units as the ratio of the two speeds) and aggregate noise (defined in dB units as “relative loss for each polarization” + “relative production rate of in-band noise photons”). This figure compares our switch to ten telecom-band switching technologies: micro-electromechanical (MEM) switches (very low speed) [6], Sagnac effect switching (very low speed) [15], polarization interferometer (low speed,

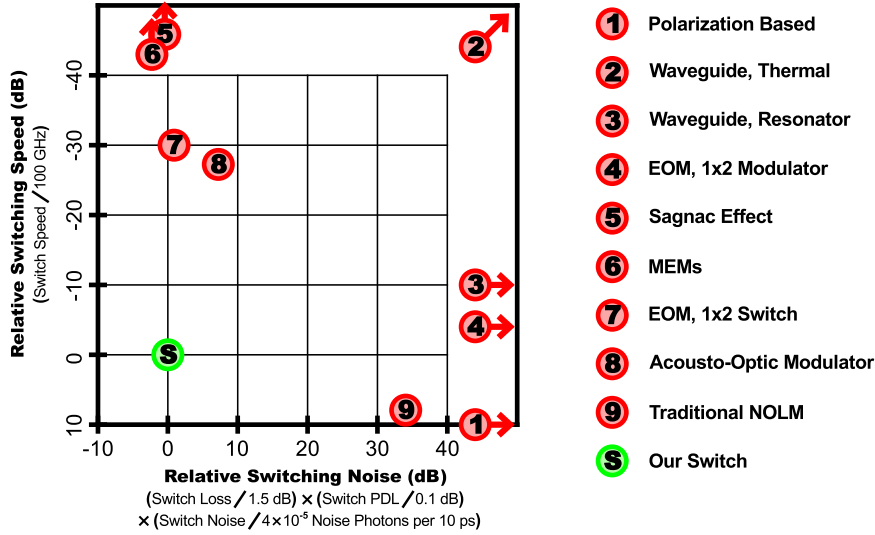


Figure 1. Relative performance of switching technologies in terms of speed (defined in dB units as the ratio of the two speeds) and aggregate noise (defined in dB units as “relative loss for each polarization” + “relative production rate of in-band noise photons”).

low bandwidth, requires phase stabilization) [16], acousto-optic modulation (low speed, low bandwidth, high loss) [21], various polarization-based switches (fundamentally single-polarization, destroying all polarization-encoded quantum information) [22], waveguide resonators (high loss, low bandwidth, single polarization) [14, 17], thermal waveguides (low speed, high loss, single polarization) [23], electro-optical modulators or EOMs (low bandwidth, single polarization) [16], and traditional nonlinear optical loop mirror (NOLM) switches (high signal band noise) [7, 19]. Considering only those categories which are essential for entangled-photon switching (speed, loss, polarization-dependence, and signal-band noise), our switching design exceeds the performance of *every* alternative—including traditional NOLM-based switches—by at least 33 dB (combined over all four categories).

Our switch is designed to operate on quantum signals (e.g., single photons) in the 1.3- μm O-band (as opposed to the 1.5- μm C-band). This choice was made for several reasons. Foremost, the dispersion minimum for standard optical fiber falls in the O-band, which avoids dispersive decoherence of the high-speed quantum signals passing through the switch. Moreover, the O-band is not only close to the loss minimum in standard optical fiber, signals in this band also traverse without loss through Erbium-doped fiber that is common in C-band optical amplifiers (see Fig. 2). Finally, because it is possible to transmit O-band entangled photons through an active C-band optical amplifier [3], it is conceivable that O-band quantum signals and C-band classical signals could co-exist in the standard telecommunications infrastructure.

Note that the traditional NOLM-based C-band devices are unsuitable for single-photon switching for two reasons: Firstly, and most importantly, such switches generate very high levels of Raman-induced background photons at signal wavelengths [20]. These

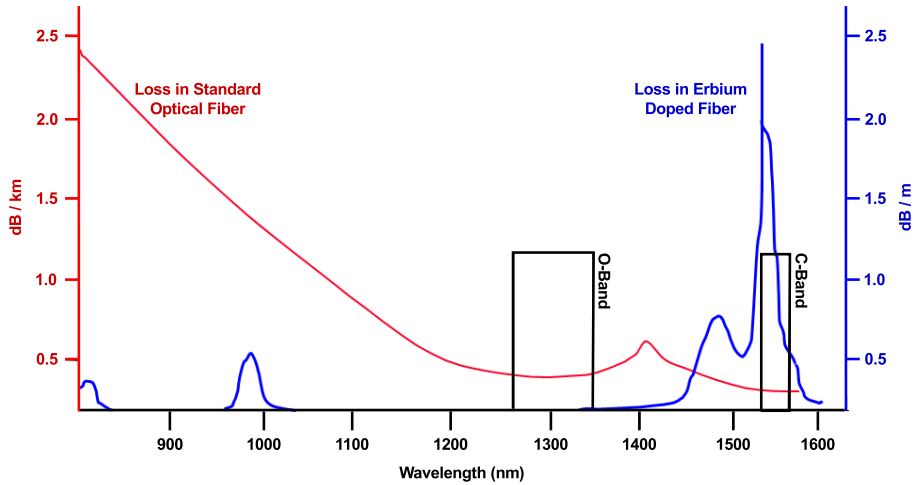


Figure 2. Absorption band of standard optical fiber (red, left ordinate) and that of Erbium-doped fiber commonly used in C-band optical amplifiers (blue, right ordinate). Notice that the 1.3- μm O-band provides minimal loss in both types of fiber.

noise photons would swamp any single-photon signals, effectively “washing out” any two-photon quantum correlations. Secondly, most NOLM-based device designs utilize pump pulses which are group-velocity matched to the signals being switched. While this increases the interaction time, the nonlinear character of the cross-phase modulation (XPM) process, on which such devices rely, limits the switching contrast in this type of operation. Because the pump pulse can not be made perfectly square-shaped, the center of the signal pulse receives a stronger nonlinear phase shift than the pulse wings, making it effectively impossible to choose a single pump power which maximizes switching contrast over the entire signal pulse.

2. Switch Design

In order to simultaneously achieve low loss and ultrafast switching, we utilize an all-optical, fiber-based design in which bright 1550-nm pump (C-band) pulses control the trajectory of 1310-nm (O-band) single-photon signals (see Fig. 3(a)). Physically, this switch exploits polarization-insensitive cross-phase modulation [24] in a nonlinear-optical loop mirror (NOLM) [25], the reflectivity of which is determined by the phase difference between the clockwise and counter-clockwise propagating paths in a fiber Sagnac interferometer (the “loop”) [26]. To actively control the state of this switch, we initially configure an intra-loop fiber polarization controller such that the loop *reflects* all incoming photons. Multiplexing a strong 1550-nm pump pulse into the clockwise or counter-clockwise loop path then creates an XPM-induced phase shift on the respective clockwise or counter-clockwise signal amplitude, with a π phase shift causing the switch to *transmit* all incoming photons.

The magnitude of this phase shift is proportional to the instantaneous intensity

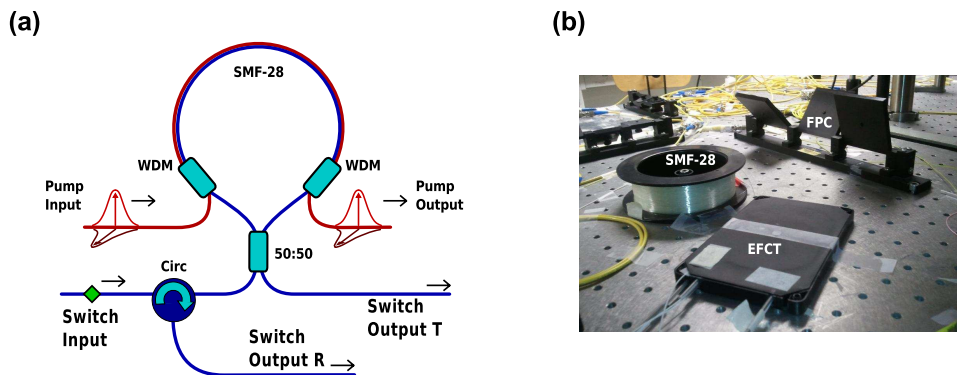


Figure 3. (a) The single-photon switch. The length of the intra-loop SMF-28 fiber is directly proportional to the switching window. An $L = 100$ -m loop results in a ≈ 200 -ps switching window. (b) A photograph of the prototype switch. The enclosed fiber component tray (EFCT) contains the 50/50 coupler, circulator, and wavelength division multiplexers. FPC, fiber polarization controller.

of the pump multiplied by the interaction time. The length of the switching loop, L , the group-velocity difference between the signal and pump pulses, $\Delta v \equiv v_s - v_p$, and the temporal profile of the pump pulse itself all affect the final temporal profile of the switching window (which as a function of time determines the probability that a signal photon will be transmitted through the switch). The group-velocity difference, in particular, is crucial for high contrast switching. Consider the example in Fig. 4.

In this diagram, the switching loop is depicted as a single straight path of length L , where the pump pulse is multiplexed into the switching fiber at $x = 0, t = 0$ and multiplexed out of the switching fiber at $x = L, t = t'$. Because in general a $\chi^{(3)}$ medium will be dispersive, we can expect there to be a non-zero difference between the pump pulse's group velocity v_p and the signal pulse's group velocity v_s . In standard fiber, 1310-nm O-band pulses travel faster than 1550-nm C-band pulses, causing an O-band pulse entering the switching region at the same time as the pump pulse to travel an additional distance Δx by the time the pump exits the switching fiber at $x = L$. Notice that in this example the first signal pulse immediately outpaces the pump pulse, implying that a cross-Kerr phase shift will only be applied to the signal near $x = 0$. A second signal pulse which enters *after* the pump pulse at a time τ_s will catch the pump at $x = L, t = t'$. A cross-Kerr phase shift will be applied to this second pulse near $x = L$. Note that the temporal extent of the *switching window* is not dependent on any specific signal pulses, or even on the existence of signal pulses. In the example above any O-band signal pulse which enters the fiber between $t = 0$ and $t = \tau_s$ will be transmitted and any which enters before or after this window will be reflected.

To calculate the walkoff time τ_s from the switching fiber parameters, first note that:

$$t' = \frac{L}{v_p} = \frac{L + \Delta x}{v_s} \quad (1)$$

and

$$\tau_s = \frac{\Delta x}{v_s}. \quad (2)$$

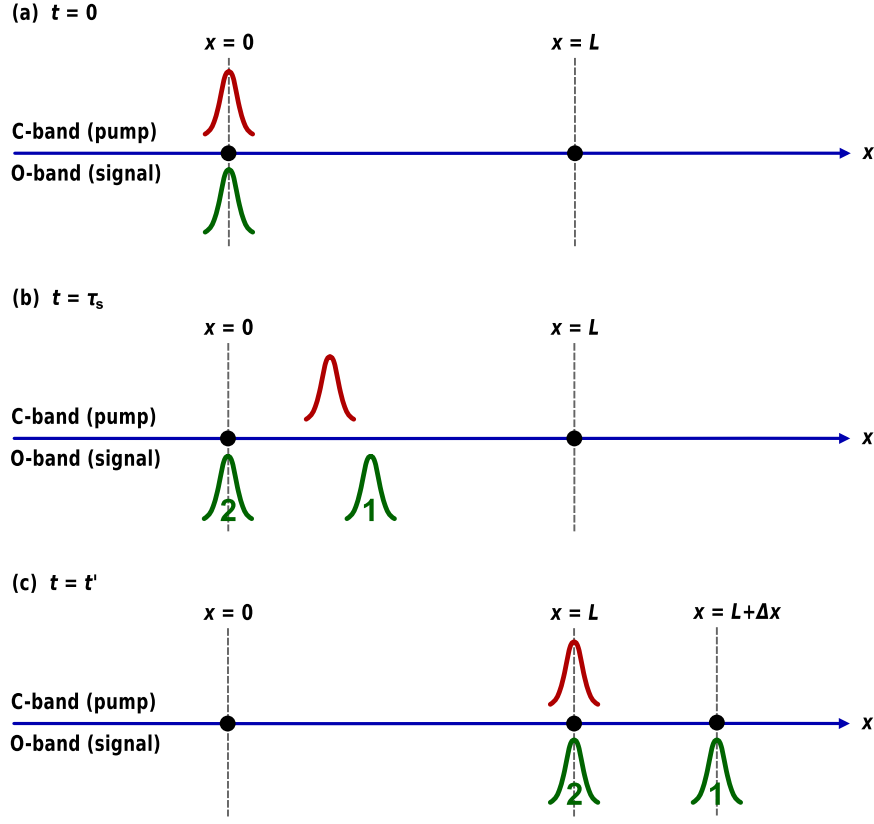


Figure 4. Pictorial diagram of a pump pulse and two signal pulses traveling clockwise through the switching loop for an example switching operation. Here the loop is depicted as a single straight path of length L , and the signal and pump pulses are assumed to have negligible temporal widths. (a) For this example, consider that the pump pulse (C-band / 1550 nm) and the first signal pulse (O-band / 1310 nm) enter the switching region (via a wavelength division multiplexer) at $t = 0, x = 0$. (b) At time τ_s , the second signal pulse enters the switching region. (c) By the time the pump pulse exits the switching region at $t = t', x = L$ (via another wavelength division multiplexer), dispersion in the fiber causes the first signal pulse to travel some additional distance Δx and the second signal pulse to exactly catch up to the pump.

By combining these two equations, we can derive an expression for τ_s in terms of L , v_s , and v_p :

$$\frac{L}{v_p} - \frac{L}{v_s} = \frac{\Delta x}{v_s} = \tau_s. \quad (3)$$

If the pump pulse is a delta function in time, the switching window is a square wave of temporal width τ_s and a height proportional to the pump intensity and inversely proportional to Δv (i.e., proportional to the nonlinear interaction time).

For real pump pulses, the switch can operate in three general regimes, depending on the pump pulse width τ_p and the walkoff time τ_s , which is in turn determined by the dispersion properties of the switching medium. If $\tau_s = 0$, which will be the case when there is no group-velocity difference between the signal and pump pulses, then the two pulses propagate in lock-step through the entire switching medium until the pump is removed via a wavelength-division multiplexer (WDM). In principle, this setting should

maximize the interaction time, making it easier to achieve the required cross-phase shift of π , while at the same time minimizing the switching window; in fact, for this case the temporal extent of the switching window will be identical to the temporal extent of the pump pulse. In practice, this configuration has a serious disadvantage, however, as real pump pulses do not have square-shaped temporal profiles but are in general Gaussian or bell-shaped. Such pulses would impart a nonuniform cross-phase shift to the signal pulse, as shown in Fig. 5(a). As τ_s increases, the temporal extent of the switching window would increase along with the pump intensity necessary to achieve a cross-phase shift of π . Eventually it approaches a critical point at $\tau_s = \tau_p$ where the relative delay accumulated between the pump and the signal pulses (inside the switching fiber) is exactly equal to the temporal extent of the pump pulse. At this point the temporal extent of the switching window is $2\tau_s = 2\tau_p$, and the cross-phase profile is still highly nonlinear. This case is shown in Fig. 5(b). If τ_s is increased to $\tau_s > \tau_p$, at least some portion of the signal will have time to completely “walk through” the pump pulse, creating a window where the cross-phase is uniform regardless of the exact shape of the pump pulse—see Fig. 5(c). As τ_s increases further, this flat cross-phase region will continue to increase. In all cases, the final cross-phase profile is equal to the convolution of the pump pulse’s temporal profile with a square wave whose width is equal to τ_s . For standard single mode fiber and for the wavelengths considered, $\tau_s \approx L \times 1.7$ ps/m.

The ability to generate a flat cross-phase profile from pump/signal walkoff is a key reason why this switch is suitable for single-photon switching while traditional C-band devices are not. Traditional C-band devices utilize non-square-wave pump pulses which are group-velocity matched to the signals being switched (the case shown in Fig. 5(a)), which makes it impossible to choose a single pump power which maximizes switching contrast over the entire signal pulse. In contrast, the large group-velocity difference between the signal and pump wavelengths (determined by the loop medium) allows our switch to operate in a regime where the pump pulse walks completely through the signal’s temporal mode, providing the type of uniform phase shift which is essential for high-contrast switching operation. The effective phase shift is therefore determined by the total energy in a single pump pulse, regardless of that pulse’s temporal profile. The switching *window*, τ , is in turn determined by the *length of the fiber* between the WDMs, L , multiplied by the speed at which the signal sweeps through the pump (for standard single-mode fiber, 1310-nm pulses have a higher group velocity than 1550-nm pulses). For our case, $\tau = \tau_s + \tau_p \approx \tau_s = L \times 1.7$ ps/m. The turn-on time of this switching window is set by the temporal extent of the pump pulses (i.e., the time it takes for the pump to physically enter and leave the fiber loop).

As XPM is inherently polarization dependent, and polarization is often used to encode quantum information, it is important that the pump pulse itself be effectively unpolarized. We accomplish this by temporally overlapping two orthogonally polarized pump pulses, each with a slightly different wavelength [24] (1545 nm and 1555 nm). In the switch described here, the dual wavelength pumps have a 1-nm bandwidth for a transform-limited turn-on time of 5 ps. If we were to instead use a 5-nm bandwidth

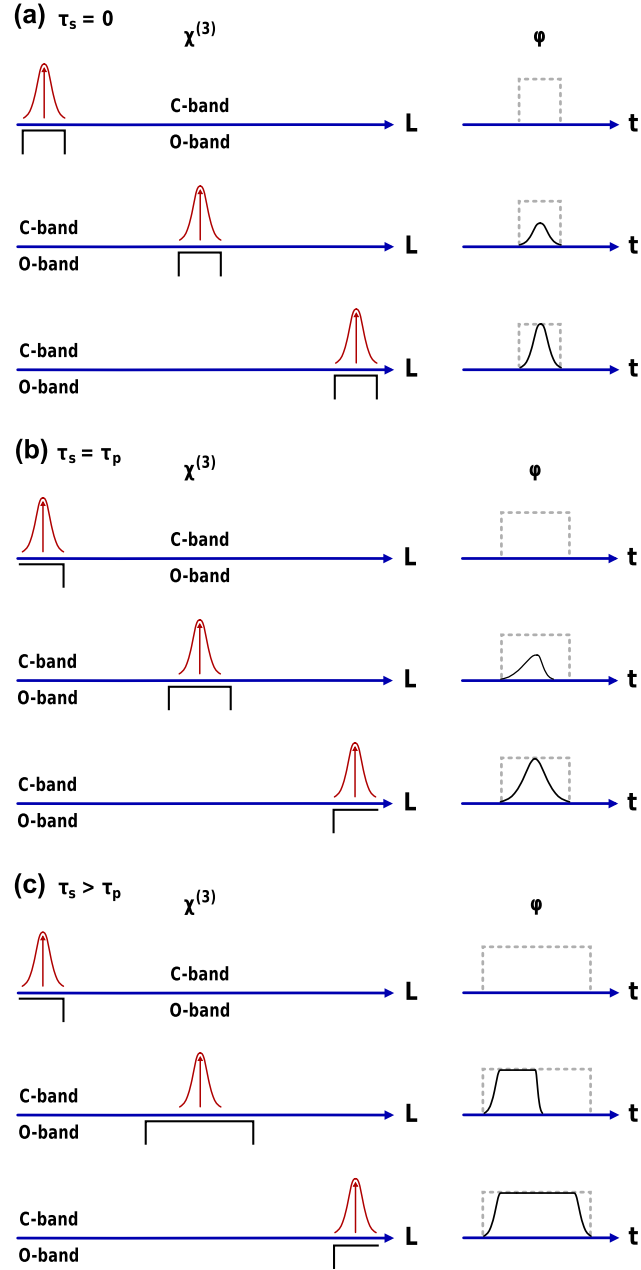


Figure 5. Pictorial diagrams of cross-phase accumulation, ϕ , in the switch as the pump (control) pulse propagates through the switching fiber for various values of τ_s . The left side shows the pump pulse relative to the target O-band switching window at various points in the switching fiber. The right side shows the accumulated cross-phase profile over the target switching window, indicated by a dotted rectangle of width $\tau_s + \tau_p$. The rectangle width indicates the target window's temporal width while its height indicates the phase necessary to attain full switching. (a) $\tau_s = 0$. The cross-phase accumulates linearly with the length of the fiber, but its shape matches that of the pump pulse's temporal profile. (b) $\tau_s = \tau_p$. The relative delay accumulated between the pump and the signal pulses is equal to the temporal extent of the pump pulse, leading to a nonuniform cross-phase shift. (c) $\tau_s > \tau_p$. Some portion of the signal window walks completely through the pump pulse, leading to a region of uniform (flat) cross-phase (i.e., uniform switching) with width $\tau_s - \tau_p$.

pump, for example, the turn-on time could be as short as 1 ps. For such pump pulses, the operation of our switch would approach the ideal, flat phase-profile regime discussed above, even for fiber lengths as short as 5 m that would lead to switching windows as short as 10 ps.

Finally, although the large group-velocity difference between 1310-nm and 1550-nm wavelengths in standard single-mode fiber (and the resulting flat switching profile) is a key advantage of this switch relative to standard C-band designs, it is not the most important advantage. The most important advantage our switch has over traditional designs is the large anti-Stokes detuning (≈ 35 THz) between the 1550-nm pump pulses and the 1310-nm single-photon pulses, which dramatically reduces contamination of the quantum channels by spontaneous Raman scattering of the pump (to a level of $\approx 2 \times 10^{-7}$ background photons per ps of the signal pulse).

3. Switch Construction

The basic components necessary to construct a Sagnac-loop based single-photon switch (see Fig. 3) include a 50/50 fiber-coupler (the entrance to the Sagnac interferometer), a pair of wavelength-division multiplexers (to add and drop the 1550-nm pump pulses), a fiber polarization controller (to configure the switch to passively reflect input light), a switching fiber (with a length L in meters equal to one-half of the desired switching window in ps), and a circulator (to redirect the reflected light). In addition, two key experimental technologies are required to operate and characterize this type of switch: a short-pulse dual-wavelength 1550-nm pump and a source of 1310-nm entangled photons.

3.1. Preparation of dual-wavelength pump pulses

Fig. 6 shows an experimental schematic of the dual-wavelength pump preparation apparatus. Two streams of 5-ps duration pulses (1545-nm and 1555-nm wavelengths) are spectrally carved with a diffraction-grating filter (DGF) from the output of a 50-MHz rate mode-locked fiber laser (IMRA Femtolite Ultra, Model BX-60), which are then multiplexed using a fiberized polarization beam combiner (FPBC). A tunable optical delay (TOD) is introduced in the path of one wavelength in order to adjust the relative timing between the two pulse streams. Another TOD is introduced after the FPBC to adjust the arrival time of the dual-wavelength pulses at the WDM in the Sagnac loop. The power necessary to produce a π phase shift is obtained by amplifying the multiplexed pulses with a cascade of erbium-doped fiber amplifiers (EDFAs). A long-pass filter (LPF) with a 1543-nm edge is used after each EDFA to ensure that the optical gain is confined to the pump pulses and that no contaminating O-band photons are introduced by the pump preparation process.

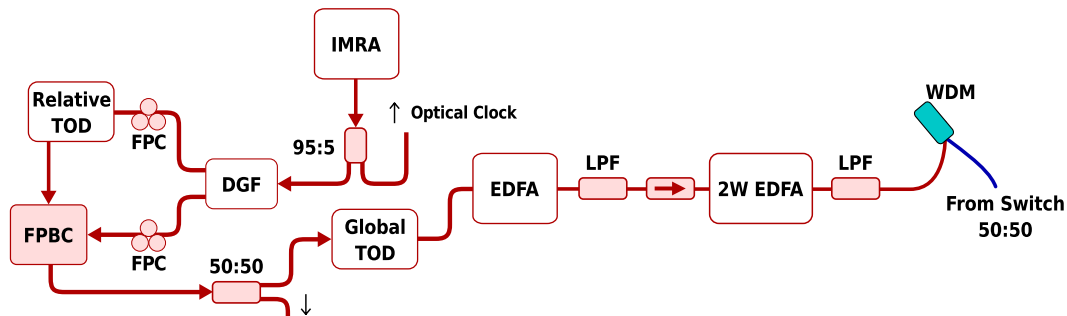


Figure 6. Experimental schematic of the dual-color pump preparation process. IMRA, femtosecond-pulse laser; DGF, double-grating filter; FPC, fiber polarization controller; TOD, tunable optical delay; FPBC, fiberized polarization beam combiner; EDFA, Erbium-doped-fiber amplifier; LPF, long-pass filter; WDM, wave-division multiplexer; and the red horizontal arrow denotes an optical isolator (a unidirectional optical device).

3.2. Entangled photon source and measurement apparatus

The IMRA laser also provides an electrical clock signal for a 1310-nm entangled photon source and an array of four single-photon detectors. The entangled photon source, shown in Fig. 7(a), utilizes spontaneous four-wave-mixing in standard single-mode fiber to produce pairs of polarization-entangled photons from 100-ps wide, 50-MHz repetition-rate pump pulses at 1305 nm. Although the photon-pair source is described in detail in [3], it is noteworthy that this type of source design is extremely robust against environmental perturbations, and is capable of producing an identical, nearly maximally entangled state without realignment for a period of several days. The results of characterizing the source over two and a half days are shown in Fig. 8. After switching, the photon pairs are measured with a correlated photon detection system (NuCrypt LLC, Model CPDS-4) consisting of an array of four InGaAs/InP avalanche photodiodes.

4. Switch Characterization

In order to test the switch’s effectiveness for quantum communications, we measured both active and passive switching of both classical pulses and polarization-entangled single-photon pairs. Figure 7(b) shows the switch as integrated into the fiber-based source of entangled photons referenced above. To test multiple switching windows, loop lengths of 500 m (≈ 900 -ps window) and 100 m (≈ 180 -ps window) were used. The insertion loss introduced by these switches in the O-band quantum channel was measured to be 1.3 dB ($L = 100$ m, port T), 1.7 dB ($L = 100$ m, port R), 1.7 dB ($L = 500$ m, port T), and 2.1 dB ($L = 500$ m, port R). Because all of these directly measured losses include the 0.4 dB or 0.8 dB loss from one or two passes through an optical circulator, the raw switching loss for either transmission through or reflection from the switching loop is 0.9 dB (1.3 dB) for the $L = 100$ -m (500-m) loop.

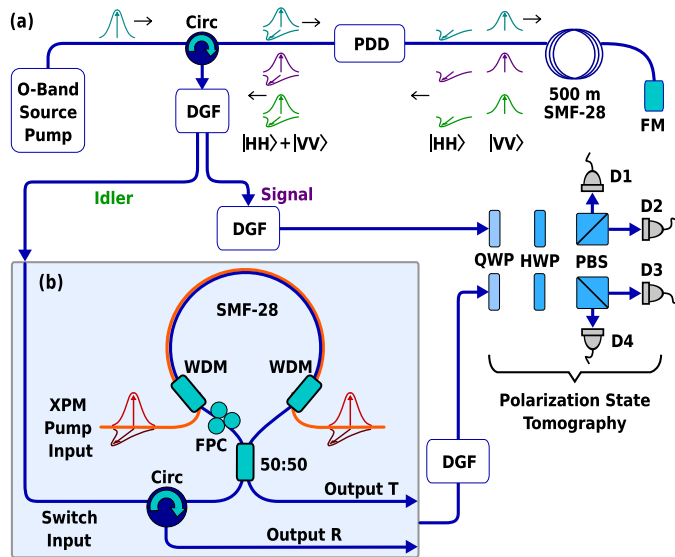


Figure 7. (a) Entangled photon-pair source and test apparatus for ultrafast switching. Nondegenerate entangled photon pairs ($\lambda_{\text{signal}} = 1303.5$ nm and $\lambda_{\text{idler}} = 1306.5$ nm) are generated in 500 m of standard single-mode fiber (SMF-28). Signal and idler photons are separated using a double-pass grating filter (DGF), with idler photons then sent to the single-photon switch. Both signal and idler photons are eventually subjected to polarization-basis tomography. Circ: circulator, FM: Faraday mirror, FPC: fiber polarization controller, HWP: half-wave plate, PBS: polarizing beam-splitter, PDD: polarization dependent delay, QWP: quarter-wave plate, WDM: wavelength-division multiplexer. (b) The single-photon switch. The length L of the intra-loop SMF-28 is directly proportional to the switching window. An $L = 100$ -m loop results in a ≈ 200 -ps switching window.

4.1. Switching contrast

An important metric for both quantum and classical routers is the switching *contrast*—the ratio of power directed to the desired output port divided by the power directed to the complementary output port. Figure 9(a) shows the classically measured switching contrast as a function of the pump-pulse energy. An optimal switching contrast of 150:1 is achieved at a pump energy of 2.5 nJ/pulse for $L = 500$ m. Although the switching contrast is expected to be independent of L , the 100-m data does not appear to achieve full contrast—only 9.2:1. This artifact is due to a long, low-power tail (≈ 370 ps total pulse width) in the 1305-nm test pulses coupled with the slow response time of the optical detectors used to collect this data. The 500-m switch opens an ≈ 1 -ns wide switching window—enough to fully switch the entire 370-ps classical pulse and thus show full contrast. The 100-m switch, however, opens a shorter, 200-ps window and can fully switch only the portion of the energy contained in that time window. Repeating these tests using single photons that are spontaneously generated from the same 1305-nm classical pulses significantly reduces the effect of this artifact—compare Figs. 9(a) and 9(b). Because the photon-pair production rate is proportional to the pump-power squared, a much smaller percentage of the generated photons resides in the tail of the pulse. Consequently, the measured single-photon switching contrasts are much closer to

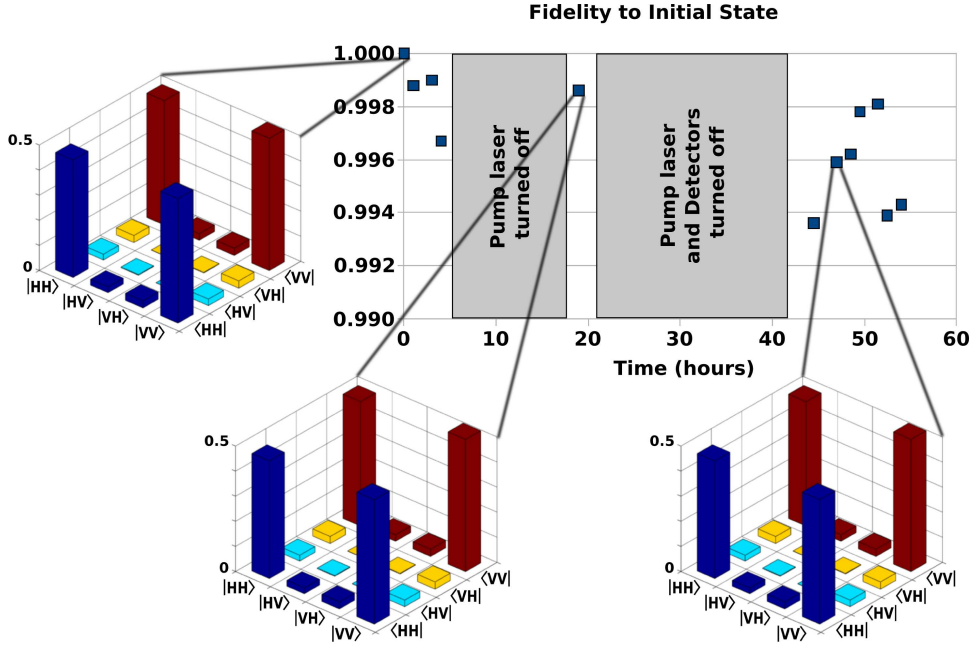


Figure 8. Source fidelity to a single maximally entangled state as a function of time. The fidelities were obtained via tomographic reconstruction of the density matrices of the entangled photons emitted by the source (a few representative density matrices are plotted as insets). Tomographic measurements were made at somewhat periodic intervals over the course of two and a half days. No realignment was performed during this period even after power cycling the pump laser (gray boxes indicate periods where the source was completely powered down).

each other, 120:1 for the 500-m switch and 43:1 for the 100-m switch (see Fig. 9(b)). We expect the true switching contrast to be the same in both cases, because the tails, although quadratically reduced, still exist in the single-photon test pulses used in these measurements.

4.2. Temporal profile of the switching operation

In addition to its use as a single-photon router, the switch is a spatio-temporal coupler, enabling the encoding and decoding of quantum information into a temporally multimode Hilbert space, which is, in principle, boundless. The extent to which this Hilbert space can be effectively accessed, however, is determined by the temporal switching profile of the device described above. In order to characterize the shape and width of the switching window, we introduce a relative delay between the signal and the pump pulse paths.

Although we are primarily interested in the switch's single-photon performance, it is useful to first characterize the switch's classical switching window. Figure 10(a) shows the measured results for 500-m, 100-m, and 2-m loop lengths, which should correspond to ≈ 850 ps, ≈ 170 ps, and ≈ 4 ps switching windows (full-width at half-maximum), respectively. Surprisingly, each of the switching windows shown in Fig. 10(a) is ≈ 150 –

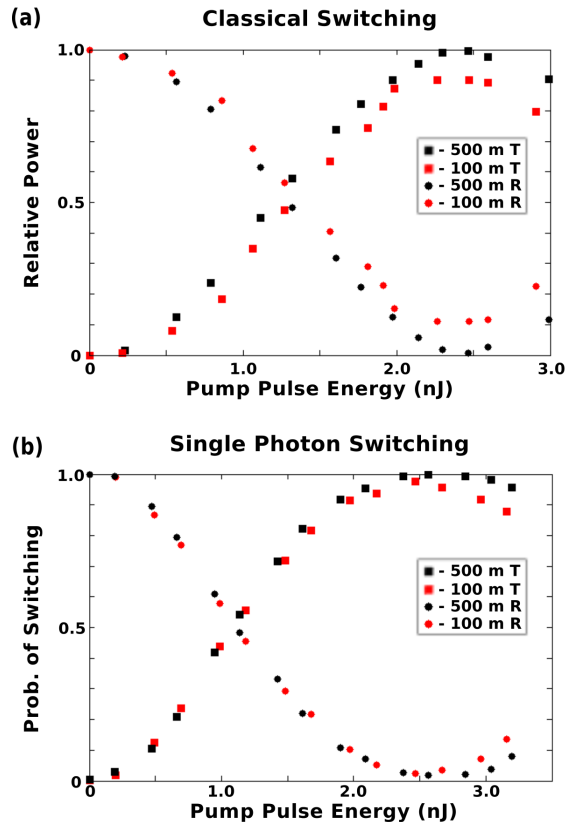


Figure 9. (a) Classical switching contrast. Plot shows normalized optical power at the switch outputs versus the energy of the 1550-nm pump pulses. (b) Single-photon switching contrast. Plot shows the probability of routing an incoming single photon versus pump energy for $L = 500$ m and $L = 100$ m (detector dark counts subtracted).

200 ps broader than these estimates, even for the 2-m switch. To understand this behavior, recall that the real switching window must be the *convolution* of the pump pulses' temporal profile (≈ 5 ps for our dual-color pump) with a square wave whose width is $\tau_s = 1.7$ ps per meter of switching fiber. The *measured* switching window, however, must be the convolution of the real switching window and *the temporal profile of the signal to be switched*. Our classical, 1305-nm test signal is in fact split from the same pump that is used in our entanglement source, i.e., the 100–200-ps pulse described above. In fact, the 2-m switching window shown in Fig. 10(a) gives us the most precise measure to date of this pulse's temporal profile.

Because the probability of generating an entangled photon pair from this pump pulse is proportional to the square of the pulse's instantaneous intensity, we can expect the single-photon switching results to exhibit slightly narrower—yet still broadened—temporal switching windows. By sweeping the relative delay while measuring the switched single photons we map the switching window and observe this effect (shown in Fig. 10(b)). As expected the temporal extent of the photons being switched blurs the true switching window. To quantitatively estimate the extent of this blurring, we use the experimentally characterized 1305-nm classical pump pulses to apply a numerical-fit deconvolution to the single-photon switching results. In this way we obtain the

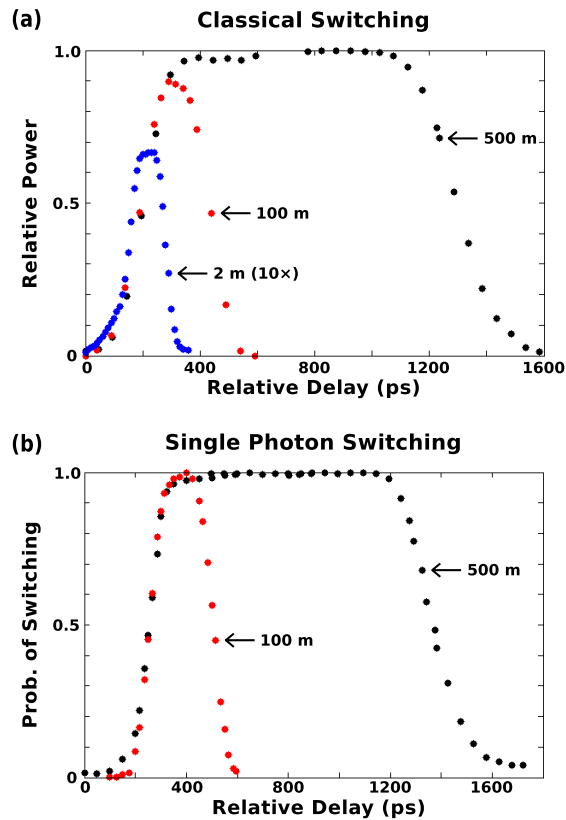


Figure 10. (a) Temporal extent of the switching window, as measured using classical test pulses. Plot shows optical power at the switch output T versus the relative delay between the pump and signal pulses (2-m loop data is shown magnified $10\times$). (b) Temporal extent of the switching window, as measured using single photons. Plot shows single-photon counts versus relative delay between the single-photon and the pump pulses (detector dark counts subtracted).

instantaneous temporal widths of the 100-m and 500-m switching windows to be 180 ps and 900 ps, respectively, as verified by the single-photon test results shown in Fig. 10(b).

4.3. Single-photon background

Closely related to contrast is the generated single-photon background, from—for example—Raman scattering of the 1550-nm pump pulses. Because any in-band single-photon background has the potential to “drown out” the entangled photons to be switched, they are a serious potential source of error. We measured the probability of generating a 1310-nm background photon count and found it to be proportional to L ($\approx 4 \times 10^{-7} \text{m}^{-1}$). Figure 11 shows the measured single-photon background counts as a function of the pump power (measured at the pump EDFA’s output, or “EDFA setting”). Because the background light is found to be proportional to the fiber length, its genesis is consistent with the Raman scattering of the pump. The negative effects of such scattering are expected to be much smaller for more advanced switches, because the chance that a background photon would be created within the mode of interest (i.e., in

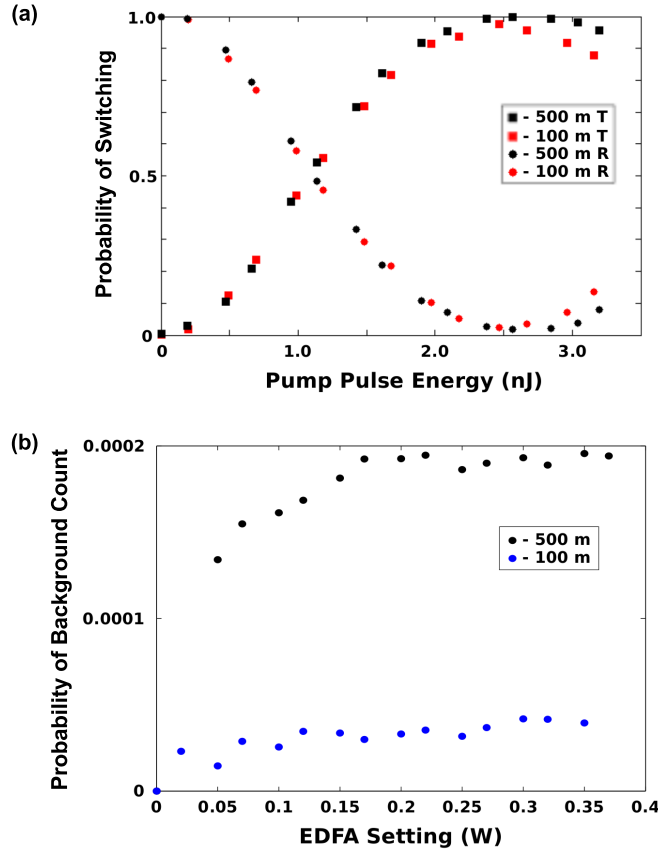


Figure 11. (a) Switching probability as a function of pump pulse energy. (b) Probability that a switching control pulse of a given energy will generate a background photon count in the 1310-nm signal band. This probability is found to be proportional to L : $\approx 4 \times 10^{-7} \text{m}^{-1}$. We note that for the two data sets shown, the pump-pulse energies plotted in (a) correspond to the EDFA settings in (b).

the same temporal mode as the pulse to be switched) may in practice be much lower than measured here, and instead be proportional to the temporal bandwidth: $\approx 2 \times 10^{-7} \text{ps}^{-1}$. This low scattering probability is consistent with the 35-THz Stokes-side detuning of the pump. Although this measured scattering probability is very low, the data is not fully described by the Raman scattering alone; for example, the scattering probability does not decrease linearly with EDFA output power but remains relatively constant. To get a clearer picture of the fundamental noise limitations of this switch, more extensive testing with additional switch-loop lengths will be required.

4.4. Switching entangled single photons

A crucial performance benchmark for the switch is its ability to route entangled photons without disturbing their quantum state. In order to measure the extent to which any disturbance occurs, we completely characterize the quantum state of unswitched entangled photons with actively switched entangled photons.

First, unswitched (no pump) entangled photons from port R are characterized

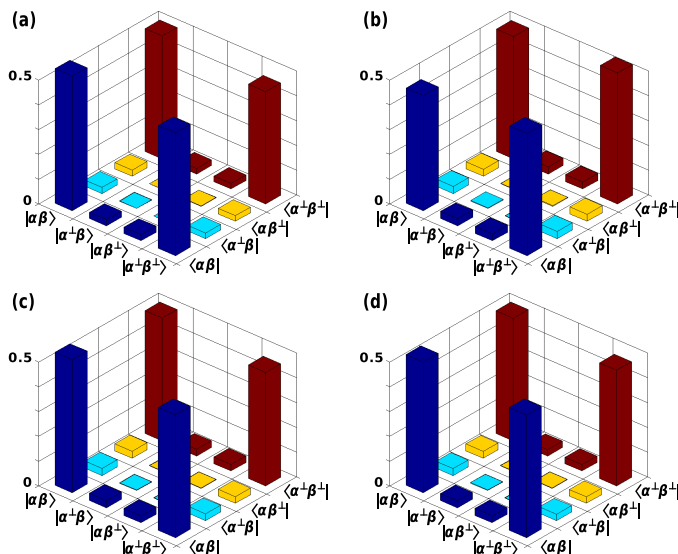


Figure 12. (a) Reconstructed density matrix of the unswitched state with the 500-m switch (fidelity to a maximally entangled state, $F = 99.5\% \pm 0.2\%$; tangle, $T = 0.982 \pm 0.005$; linear entropy, $S_L = 0.0005 \pm 0.003$). (b) Reconstructed density matrix of the switched state from the 500-m switch ($F = 99.2\% \pm 0.2\%$, $T = 0.967 \pm 0.007$, $S_L = 0.01 \pm 0.005$). (c) Reconstructed density matrix of the unswitched state for $L = 100$ -m ($F = 99.5\% \pm 0.2\%$, $T = 0.981 \pm 0.01$, $S_L = 0.001 \pm 0.004$). (d) Density matrix of the switched state for $L = 100$ m ($F = 99.4\% \pm 0.4\%$, $T = 0.978 \pm 0.01$, $S_L = 0.005 \pm 0.01$).

followed by actively switched entangled photons from port T. In both cases we use coincidence-basis quantum-state tomography [27, 28]. Both signal and idler photons are analyzed using separate quarter-waveplate (QWP), half-waveplate (HWP), and polarizing-beam-splitter (PBS) combinations, which together perform arbitrary single qubit measurements. The measured coincidence rates—after subtracting accidental coincidences, a procedure which lowers statistical errors [29]—for 36 combinations of analyzer settings [30] are subjected to a numerical maximum likelihood optimization, which reconstructs the density matrix most likely to have produced the measured results. Figures 12(a) and 12(b), respectively, show the reconstructed density matrices for passively switched (port R) and actively switched (port T) entangled photons, after reflection or transmission through the $L = 500$ -m loop. Similar reconstructions for the $L = 100$ -m loop are shown in Figs. 12(c) and 12(d); in all four cases, the fidelity of the measured state to a maximally-entangled state exceeds 99.0%. In addition, no measurable state degradation results from active versus passive switching.

4.5. Polarization dependence

The quantum state tomography tests described above provide some evidence that the switch is polarization independent (because a strong polarization dependence would lead to a degradation in the polarization entanglement). To perform a more thorough study of the switch's polarization dependence, we introduce a 1-m (≈ 5 ns) delay into the 1545-

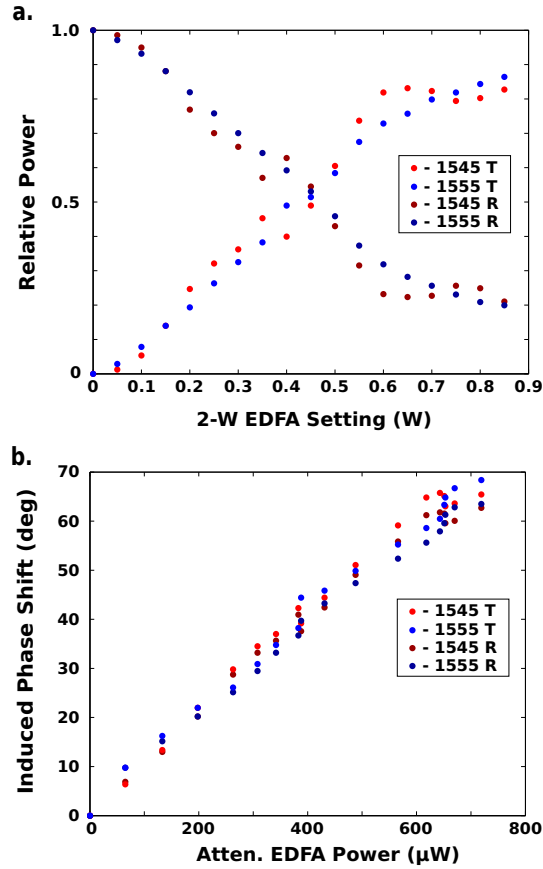


Figure 13. Experimental results for the switch with the two colors of the XPM pump temporally separated. (a) Normalized power of the O-band signal reflected and transmitted by the temporally separated 1545-nm and 1555-nm XPM pump pulses versus the EDFA power settings. (b) Computed phase-shift applied by each color of the XPM pump for the measured EDFA powers.

nm arm of the grating filter used to generate the two-color XPM pulses. By reverting to a continuous wave (CW) O-band signal, the switching performance for each color of the switching pulse can be independently monitored as their polarizations are rotated using a single FPC. Additionally, adjusting the signal FPC does not change the switched output from either pump-color/polarization by more than 20%. This small change is attributed to the different birefringence-induced polarization rotations experienced by the O-band versus the C-band light. In other words, even a single-polarization pump pulse may have its polarization rotated relative to a given signal pulse, resulting in relatively polarization-independent switching for a single-color pump. However, we anticipate that single-color-pump devices will become more polarization dependent as the switching window is reduced (i.e., as L is decreased).

Next, the two time-delayed pump powers are balanced and both output ports of the switch are monitored on 1-GHz-bandwidth photodiodes connected to the same oscilloscope, while the switch is initially set to reflect the entire incoming CW signal. In this way we can monitor the relative strength of the signal output pulses for a range of

EDFA settings; the results are plotted in Fig. 13(a). Measuring the relative signal values at the reflected and transmitted ports allows us to calculate the optical phase imparted by either pump color through the XPM process, as shown in Fig. 13(b). The agreement between the calculated values of the cross-phase shift from the transmitted and reflected ports for both pump colors provides strong evidence that the results are interpreted correctly. It further shows that, when the two pump colors are recombined (by removing the 1-m delay), the resulting pump pulses would act as the desired depolarized XPM pump. It also confirms that the EDFA provides a relatively constant gain for both colors of the XPM pump.

5. Demultiplexing a Dual-Channel Entangled Photon Stream

The switch's ability to manipulate spatial and temporal quantum information has the potential to enable new quantum communication protocols and new quantum networks. As an example of this functionality, we use the switch to demultiplex a single quantum channel from a dual-channel entangled photon stream. The goal of this experiment is to demonstrate a time-division-multiplexed (TDM) single-photon quantum channel operating at 3-GHz. To simulate this type of quantum network, we encode two maximally entangled photon pairs into adjacent temporal modes, separated by 300 ps. After demonstrating that each of the adjacent temporal modes contains a different maximally entangled state (see Figs. 17(a) and 17(b)), we measure both modes simultaneously, which results in a low-entanglement mixture of the two different maximally entangled states (see Fig. 17(c)). Finally, we use our single-photon switch to demultiplex the two modes, recovering a single-channel's maximal entanglement (Fig. 17(d)).

For this test, we encode the dual-channel entangled state into a five-qubit Hilbert space (see Fig. 14) defined by the signal and idler polarization qubits ($|H^{s,i}\rangle, |V^{s,i}\rangle$), the signal and idler temporal qubits ($|t_0^{s,i}\rangle, |t_1^{s,i}\rangle$), and an idler spatial qubit ($|T^i\rangle, |R^i\rangle$) (see Fig. 7(b)). Using this encoding, we create the five-qubit hyper-entangled state

$$|\Phi\rangle = c_1|\psi_1\rangle|t_0^s\rangle|t_0^i\rangle|T^i\rangle + c_2|\psi_2\rangle|t_1^s\rangle|t_1^i\rangle|T^i\rangle, \quad (4)$$

where

$$|\psi_1\rangle \equiv \frac{1}{\sqrt{2}} \left(|H^s\rangle|H^i\rangle + |V^s\rangle|V^i\rangle \right), \quad (5)$$

$$|\psi_2\rangle \equiv \frac{1}{\sqrt{2}} \left(|H^s\rangle|H^i\rangle - |V^s\rangle|V^i\rangle \right), \quad (6)$$

and c_1 and c_2 are arbitrary coefficients. Measuring $|\Phi\rangle$ using polarization-basis tomography while *tracing out* temporal degrees of freedom and *projecting* into the idler spatial mode $|T^i\rangle$ will yield a highly mixed state, exactly the result one expects from a simultaneous measurement of multiple entangled quantum channels. A switch capable of implementing a controlled-NOT operation which couples the spatial and temporal qubits (see Fig. 14), however, would transform $|\Phi\rangle$ into the state:

$$|\Phi'\rangle = c_1|\psi_1\rangle|t_0^s\rangle|t_0^i\rangle|T^i\rangle + c_2|\psi_2\rangle|t_1^s\rangle|t_1^i\rangle|R^i\rangle. \quad (7)$$

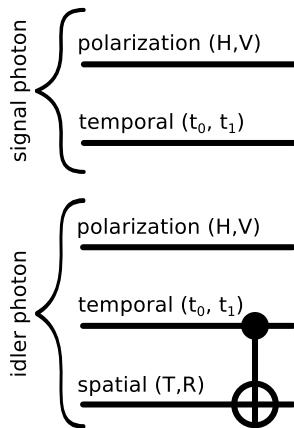


Figure 14. Diagram of the five degrees of freedom in a multiplexed entangled photon stream, which can be demultiplexed by applying the controlled switch operation (shown).

This demultiplexed state should exhibit maximal entanglement when *projected* into the spatial mode $|T^i\rangle$, because even after tracing over the temporal degrees of freedom only the maximally entangled polarization state $|\psi_1\rangle$ would be present.

5.1. Generating a dual-channel entangled photon stream

To implement this proof-of-principle test of the switch’s ability to couple spatial and temporal degrees of freedom, we modify our O-band entangled-photon source [3] by pumping it with a pair of pulses separated by $\Delta t \equiv t_1 - t_0 \approx 300\text{ps}$. Fig. 15(a) shows a diagram of the interferometer used to delay one pump pulse relative to the other, while Fig. 15(b) shows a pictorial view of the creation of the dual-channel entangled photon stream. Note that the same input pump pulse is split with a Michelson-type interferometer with an additional quarter waveplate in each arm. These quarter waveplates are aligned so as to minimize the light reflected back through the initial PBS from one arm and to cut the reflected light in half from the other. Such settings lead to one vertically polarized pump pulse and one diagonally polarized pump pulse temporally separated by ≈ 300 ps. By choosing these polarizations for the leading and trailing pump pulses (and after transmitting them through additional in-fiber polarization rotations) the resulting pump state is $\sqrt{c_1}(|H^p\rangle + |V^p\rangle)t_0 + \sqrt{c_2}(|H^p\rangle + i|V^p\rangle)t_1$, which upon SFWM gives the output signal-idler state $|\Phi\rangle$. For the demultiplexing test, we choose $c_1/c_2 \approx 1.25$ and $\Delta t \approx 300$ ps. An experimental schematic for this type of pump preparation and entangled photon generation is shown in Fig. 15.

Next, we determine the appropriate setting of the global delay in the XPM pump path. We actively switch the idler channel to port T and then measure the coincidences between the signal and idler channels while blocking exactly one arm of the Michelson interferometer shown in Fig. 15(a). By recording coincidence counts for each configuration as a function of the global pump delay, we are able to reconstruct two curves which are analogous to a classical “eye diagram”; as shown in Fig. 16. Setting

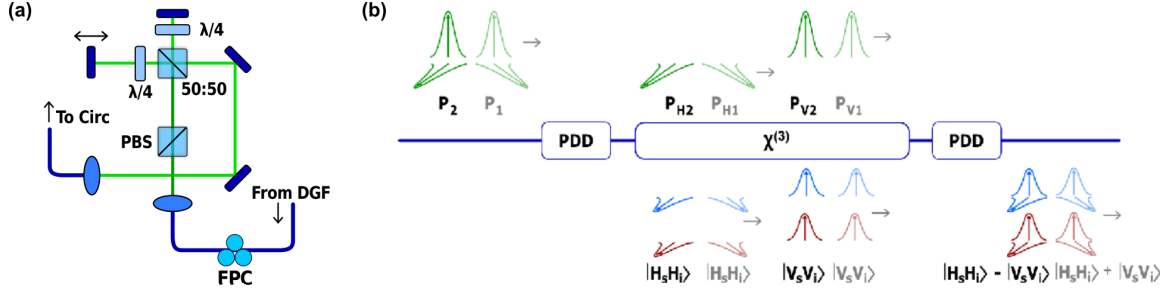


Figure 15. (a) Michelson interferometer used for preparing the SFWM pump to generate time-division-multiplexed entangled photons. (b) Pictorial diagram of the SFWM processes which produce the time-division-multiplexed entangled photon stream.

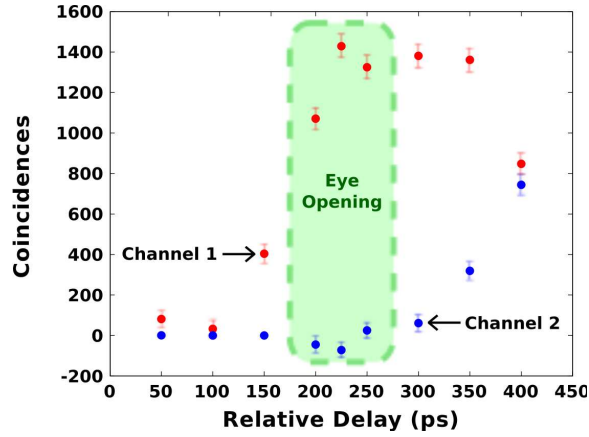


Figure 16. Temporal profiles of the two independent channels in a dual-channel entangled photon stream. A single channel (either 1 or 2) is measured by blocking one arm of the Michelson interferometer (see Fig. 15(a)) used to create the dual-channel entangled photon source, in effect altering the source to create only a single temporal channel of the entangled photon pairs. The temporal profile of a single entangled-photon channel is recorded using the $L = 100$ m switching device described above, configured to transmit any signal photons which arrive during the 200-ps switching window defined by the C-band switching pulse. By recording the accidental-subtracted coincidence counts as a function of the C-band pulse’s arrival time (controlled using the global TOD in the XPM pump path—see Fig. 6), we can map the temporal profile of each channel. The red datapoints correspond to the state depicted in Fig. 17(a) while the blue datapoints correspond to the state depicted in Fig. 17(b). By placing the global XPM-pump delay in the central region marked with a green dashed box and unblocking both arms of the source Michelson interferometer, we are able to demultiplex channel 1 from channel 2. The behavior shown here is equivalent to a classical switching “eye diagram”.

the delay to 225 ps, we achieve full switching of the coincidences of the first temporal channel, with minimal contribution from the second.

5.2. Demultiplexing results

Figure 17(c) shows the experimentally measured density matrix for the multiplexed quantum channels. As expected, the state is highly mixed; its fidelity to the nearest

maximally entangled state is only 58.9%. Utilizing the 100-m switch we then demultiplex (i.e., actively switch) only the first quantum channel ($t = t_0$), creating the state $|\Phi'\rangle$. As shown in Fig. 17(d), after demultiplexing we are able to recover the high fidelity (98.6%) of the target state to a maximally entangled state. Because the cross-Kerr phase shift has previously been shown to maintain spatial and temporal coherence in NOLM switches [7, 19], we anticipate that this switch’s cross-Kerr-based demultiplexing operation is in fact coherent and equivalent to the controlled-NOT operation depicted in Fig. 14 (although measurements equivalent to a full three-qubit process tomography would be necessary to show this conclusively). Moreover, unlike LOQC-based controlled-NOT gates, this switch is completely deterministic and easily extensible, capable of independently tunable couplings (e.g., controlled- $\pi/4$) to many temporal qubits encoded onto the same photon (by changing the control-pulse’s intensity as a function of time). By cascading several switches, it is also possible to couple to multiple spatial qubits.

6. Conclusion

We have demonstrated the first all-optical switch suitable for single-photon quantum communications. It achieves low-loss (< 1 dB when used to switch between transmitted and reflected modes, < 1.7 dB when combined with a circulator), high-isolation (> 20 dB), and high-speed (< 200 ps) performance without a measureable disturbance to the quantum state of the routed single photons. We demonstrate its ultrafast capability by demultiplexing a single quantum channel from a time-division-multiplexed stream of entangled photons. Very few fundamental limitations apply to this type of switch design. With carefully designed fiber components, one has the potential to dramatically reduce the switch’s loss. In principle the only unavoidable switching losses are fiber transmission losses (0.15–0.2 dB/km) and circulator insertion losses (waveguide-based circulators with a 0.05 dB insertion loss have been designed and simulated [31]). Additionally, decreasing L to a few meters will reduce the switch’s speed to ≈ 10 ps while simultaneously decreasing the background by an order of magnitude. Even without these improvements, however, this switch represents an important new tool for manipulating spatially- and temporally-encoded quantum information.

This research was supported in part by the DARPA ZOE program (Grant No. W31P4Q-09-1-0014) and the NSF IGERT Fellowship (Grant No. DGE-0801685).

References

- [1] M. A. Nielsen and I. L. Chuang, *Quantum Computation and Quantum Information* (Cambridge Univ. Pr., 2000).
- [2] N. I. Nweke, *et al. Appl. Phys. Lett.* **87**, 174103 (2005).
- [3] M. A. Hall, J. B. Altepeter, and P. Kumar, *Optics Express* **17**, 14558 (2009).
- [4] M. A. Duguay and J. W. Hansen, *Appl. Phys. Lett.* **15**, 192 (1969).
- [5] N. J. Doran, and D. Wood, *Opt. Lett.* **13**, 56–58 (1988).
- [6] K. Hogari and T. Matsumoto, *Appl. Opt.* **30**, 1253–1257 (1991).
- [7] M. Eiselt, *Electron Lett.* **28**, 1505 (1992).

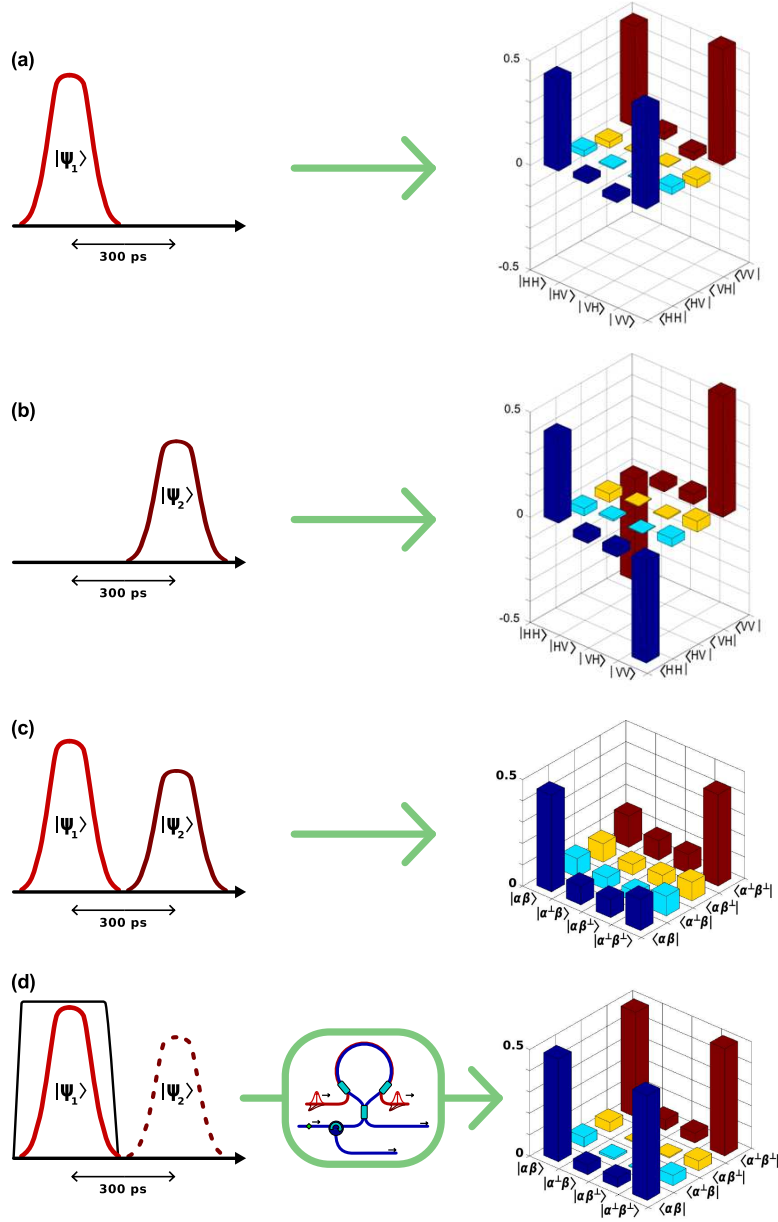


Figure 17. Pictorial description of the construction and demultiplexing of a dual-channel entangled photon stream. (a) Channel 1, containing the entangled state $|\psi_1\rangle \equiv \frac{1}{\sqrt{2}} (|H^s\rangle|H^i\rangle + |V^s\rangle|V^i\rangle)$ (fidelity to a maximally entangled state $F > 99\%$). (b) Channel 2, containing the entangled photon state $|\psi_2\rangle \equiv \frac{1}{\sqrt{2}} (|H^s\rangle|H^i\rangle - |V^s\rangle|V^i\rangle)$ ($F > 99\%$). (c) Multiplexed channels, defined by the five-qubit state $|\Phi\rangle = c_1|\psi_1\rangle|t_0^s\rangle|t_0^i\rangle|T^i\rangle + c_2|\psi_2\rangle|t_1^s\rangle|t_1^i\rangle|T^i\rangle$. By tracing over the temporal degree of freedom and projecting into the spatial mode $|T^i\rangle$, we reconstruct a highly mixed density matrix with dramatically reduced state fidelity ($F = 58.9\% \pm 0.5\%$). (d) De-multiplexed channel. By actively switching the channel 1 idler photons to output T, c.f. Fig. 7(b) (i.e., demultiplexing channel 1), we can project into spatial mode $|T^i\rangle$ and recover the maximally entangled state $|\psi_1\rangle$ ($F = 98.6\% \pm 0.7\%$).

- [8] J. P. Sokoloff, P. R. Prucnal, I. Glesk, M. Kane, *IEEE Photon. Technol. Lett.* **5**, 787 (1993).
- [9] M. Asobe, I. Yokohama, H. Itoh, and T. Kaino, *Opt. Lett.* **22**, 274 (1997).
- [10] I. Yokohama *et al.*, *J. Opt. Soc. Am. B* **14**, 3368 (1997).
- [11] G. S. Kanter, P. Kumar, K. R. Parameswaran, and M. M. Fejer, *IEEE Photon. Technol. Lett.* **13**, 341 (2001).
- [12] J. E. Sharping, M. Fiorentino, P. Kumar, and R. S. Windeler, *IEEE Photon. Technol. Lett.* **14**, 77 (2002).
- [13] V. Van, *et al.* *IEEE Photon. Technol. Lett.* **14**, 74 (2002).
- [14] V. R. Almeida *et al.*, *Opt. Lett.* **29**, 2867–2869 (2004).
- [15] G. Bertocchi, *et al.* *J. Phys. B* **39** 1011 (2006).
- [16] <http://www.eospace.com>
- [17] P. Dong, S. F. Preble, and M. Lipson, *Opt. Express* **15**, 9600–9605 (2007).
- [18] C. Knoernschild, C. Kim, F. P. Lu, and J. Kim, *Opt. Express* **17**, 7233–7244 (2009).
- [19] K. Uchiyama *et al.*, *J. Lightw. Tech.* **15**, 194–201 (1997).
- [20] Q. Lin, F. Yaman, and G. P. Agrawal, *Phys. Rev. A* **75**, 023803 (2007).
- [21] <http://www.sintecoptronics.com/>
- [22] S. Kinoshita *et al.*, *Rev. Sci. Instrum.* **71**, 3317 (2000).
- [23] I. Kiyat, A. Aydinli and N. Dagli, *Photonics Technology Letters*, IEEE, **18** 364–366 (2006).
- [24] H. Bülow and G. Veith, *Elect. Lett.* **29**, 588–589 (1993). Note that if one of the two pump colors leads the other by a time δ , then the leading and trailing δ -length segments of the switching window will not be polarization-independent.
- [25] K. J. Blow, N. J. Doran, B. K. Nayar, and B. P. Nelson, *Opt. Lett.* **15**, 248–250 (1990).
- [26] D. Mortimer, *J. Lightw. Tech.* **6**, 1217–12124 (1989).
- [27] D. F. V. James, P. G. Kwiat, W. J. Munro, and A. G. White, *Phys. Rev. A* **64**, 052312 (2001).
- [28] J. B. Altepeter, E. R. Jeffrey, and P. G. Kwiat, *Advances in AMO Physics*, Vol. 52, Ch. 3 (Elsevier, 2006).
- [29] Increasing this source’s pair production rate (PPR) and then subtracting accidental coincidences increases measurement precision while accurately predicting the low-PPR, non-accidental subtracted result [3]. Without this correction, high-PPR, dark-count-only subtracted fidelities for the data shown in Figs. 1 and 3 are between 80–95%.
- [30] J. B. Altepeter, *et al.* *Phys. Rev. Lett.* **95**, 033601 (2005).
- [31] R. Takei and T. Mizumoto, *Jpn. J. Appl. Phys.* **49**, 052203 (2010).